Scalar-type gravitational wave emission from gravitational collapse in Brans-Dicke theory: Detectability by a laser interferometer

Masaru Shibata
Department of Earth and Space Science, Faculty of Science, Osaka University, Toyonaka, Osaka 560, Japan

Kenichi Nakao
Department of Physics, Kyoto University, Kyoto 606-01, Japan

Takashi Nakamura
Yukawa Institute for Theoretical Physics, Kyoto University, Kyoto 606-01, Japan
(Received 24 May 1994)

To investigate the possibility of obtaining evidence for scalar-tensor theories of gravity by laser interferometric gravitational wave observatories (e.g., LIGO), we perform numerical simulations of the gravitational collapse of a spherically symmetric dust fluid and investigate the waveform and amplitude of scalar-type gravitational waves (SGW's) in the Brans-Dicke theory, which is one of the simplest scalar-tensor theories. We find that in the case of the dust collapse of mass $\sim M_\odot$ and initial radius $\sim$ 100–1000 km, the emitted SGW's have a maximum amplitude $\sim 10^{-22}(500/\omega)$ (10 Mpc/R) and a characteristic frequency $\sim$ 40–1000 Hz. This means that if the gravity theory is the Brans-Dicke theory with $\omega \lesssim$ several thousands, the advanced LIGO may detect a signal of SGW's from a supernova at the Virgo cluster. And, if we happen to find a supernova in our Galaxy, we may detect SGW's even if ω is as large as $\sim 10^6$. Concerning cosmic censorship, we also investigate the fate of a collapsed object. Our numerical results suggest that the final product of a collapsed object is a black hole in the Brans-Dicke theory like in the Einstein theory, and outside the black hole, the Brans-Dicke scalar field seems to become constant. These results support the cosmic censorship conjecture.

PACS number(s): 04.30.Db, 04.50.+h

I. INTRODUCTION

Laser interferometric gravitational wave observatories (such as LIGO) will be in operation by the end of this century [1]. These detectors have the ability to detect the signal of gravitational waves from coalescing binaries with an amplitude $\gtrsim 10^{-23}$ and frequency 10–1000 Hz. Using the matched filter technique [2,3] in the data analysis, we have a chance to determine not only the various parameters of a binary, such as mass, spin [4,5], inclination [6], radius of neutron stars [3], and so on, but also to obtain the cosmological parameters such as the Hubble constant H_0, cosmological constant Λ, and the deceleration parameter q_0 [7,8]. It may be possible to identify the γ-ray burst with coalescing binary neutron stars [9]. These show that the observation of gravitational waves is very important for astronomy because it allows us a new way to see the Universe as a whole as well as the general relativistic objects themselves, such as neutron stars and black holes. But here we point out other possibilities by the detection of gravitational waves.

Can we use gravitational waves to verify Einstein's theory of gravity? Of course there are no experiments that contradict Einstein's theory of gravity [10], but all tests except for the pulsar timing test [11] are within the parametrized post-Newtonian (PPN) framework, which have fundamental limitations because they test objects in weak gravity. From a quantum theoretical point of view, the Einstein theory should be regarded as an effective theory in the energy scale much lower than the Planck scale. Hence, it is a natural question as to whether or not the Einstein theory is a good effective theory even in strong gravity systems in which the PPN framework is not applicable.

As an example for the other metric theories of gravity, dilaton gravity is naturally predicted by the superstring theory, which is at present only one theory to treat the gravity in a way consistent with quantum mechanics [12]. Dilaton gravity is included in a more general framework, i.e., the so-called scalar-tensor theory. In practice, we have not yet been able to rule out the scalar-tensor theories, and also vector-tensor theory [10], because such theories have the allowed regions for their intrinsic parameters (e.g., ω in the Brans-Dicke theory [13], which is the simplest one in the scalar-tensor theories). To verify the correctness of the Einstein theory more rigorously or to obtain evidence for the other metric theories, we need other tests involving a strong gravity source such as black holes and neutron stars.

One method is the pulsar timing test in a binary pulsar [11] in which the total energy of the system is dissipated by the emission of gravitational waves. The essence of this method is that each theory predicts different polarizations of gravitational waves and, as a result, a different emissivity of gravitational waves. Since pulsar timing is affected by the back reaction of gravitational waves, each theory predicts a different pulsar timing. Hence, making

use of the binary pulsar, especially using a black-hole–neutron-star binary pulsar, we can test the metric theory more rigorously [10,14]. However, for a rigorous test, we need black-hole–neutron-star binaries or binary neutron stars of a large mass ratio in our Galaxy [14], which have not been found yet.

The second possibility to investigate the metric theory is the direct detection of gravitational waves, which may include various types of polarization [15,16]. For example, let us consider the Brans-Dicke theory (or scalar-tensor theory), which is our subject in this paper. In this case, there are three polarization modes: Two of them are the same as those in the Einstein theory, that is, the so-called + and × modes, but there exists one additional mode, the scalar (spin-zero) mode, *which is emitted even in the spherically symmetric space-time.* Thus, theoretically, if we can detect scalar-type gravitational waves (SGW's) with a laser interferometric detector, we may say that the scalar-tensor theory is correct. Also, if we do not detect the scalar mode but do detect only + and × modes, it has an important meaning because we can exclude the scalar-tensor theory within the sensitivity of the detector.

In practice, there may be maximally six polarization modes in gravitational waves if we take into account the various theories [15,10]. In this case we need at least six detectors operating at the same time and at different places to distinguish every mode. Hence, it seems impossible to distinguish the scalar mode from the various other modes unless we find a strong periodic source of gravitational waves [10]. However, as shown in this paper, the characteristic amplitude and frequency of the scalar mode may be different from those of the other modes in some sources of gravitational waves. This means that several characteristic peaks may appear in the spectrum of gravitational waves. Since the interferometric gravitational wave detector has a wide frequency band, it has the ability to detect the various types of waves of different characteristic frequencies and waveforms. Hence, we may be able to distinguish the scalar mode from the other modes completely by making use of the features of these modes.

From the above point of view, a supernova (SN), which is considered a weak emitter of gravitational waves in the case of the Einstein theory [17], becomes an important source of SGW's because the scalar mode is emitted even from spherically symmetric collapse. We can think as follows: If signals of SGW's from a SN are detected, we can verify the scalar-tensor theory, and, even if no signals of SGW's are detected from the SN, which is seen by electromagnetical observations, we may give the upper limit of the intrinsic parameter of the theory, e.g., ω in Brans-Dicke theory. Thus, the absence of a signal may lead to the restriction of the theory.

This is the reason we perform the numerical simulation of the gravitational collapse and investigate the amplitude and the frequency of SGW's in the Brans-Dicke theory to see the possibility in detecting gravitational waves other than the + and × modes. Although there are many alternative scalar-tensor theories in addition to the Brans-Dicke theory, which is consistent with the PPN experiment [10,18], we only pay attention to the Brans-Dicke theory because our intent here is to show that it is possible to detect SGW's from the SN source. Hence, we also do not intend to calculate the detailed dynamics of the gravitational collapse and waveforms of SGW's. The detailed calculations will be future problems.

The remainder of this paper is devoted to the details underlying the above discussion. In Sec. II, we derive the equations for the spherical symmetric gravitational collapse in the Brans-Dicke theory, and the numerical methods are also shown. In Sec. III we first show the numerical results, in particular, the waveforms and the Fourier spectra of SGW's for various models. Even if the SGW has a high enough amplitude to be detected by the interferometric detector, it is nontrivial whether or not the detector has the ability to detect SGW's. Thus, in the latter half of Sec. III, we show that it is possible to detect SGW's with a laser interferometric detector. To make sure of the cosmic censorship hypothesis [19], in Sec. IV, we briefly show that the final fate of the collapsing objects is a black hole by means of the apparent horizon search. Section V is devoted to the summary. Throughout this paper, we take the units of $c = G = 1$ and $M_\odot$ denotes the solar mass.

II. BASIC EQUATIONS AND NUMERICAL METHOD

A. Basic equations

The basic equations of the Brans-Dicke theory [13] are originally expressed in the Brans-Dicke frame, and they have the form

$$\hat{R}_{ab} - \tfrac{1}{2}\hat{g}_{ab}\hat{R} = 8\pi\phi^{-1}\hat{T}_{ab} + \omega\phi^{-2}(\hat{\nabla}_a\phi\hat{\nabla}_b\phi - \tfrac{1}{2}\hat{g}_{ab}\hat{g}^{cd}\hat{\nabla}_c\phi\hat{\nabla}_d\phi) + \phi^{-1}(\hat{\nabla}_a\hat{\nabla}_b\phi - \hat{g}_{ab}\hat{\nabla}_c\hat{\nabla}^c\phi) , \quad (2.1)$$

$$\hat{\nabla}_a\hat{\nabla}^a\phi = 8\pi(2\omega+3)^{-1}\hat{T}^a_a , \quad (2.2)$$

and

$$\hat{\nabla}_a\hat{T}^a_b = 0 , \quad (2.3)$$

where $\hat{g}_{ab}$ is the metric in the Brans-Dicke frame, and $\hat{R}_{ab}$, $\hat{R}$, and $\hat{\nabla}$ are the Ricci tensor, Ricci scalar, and covariant derivative with respect to $\hat{g}_{ab}$, respectively. $\hat{T}_{ab}$ is the energy-momentum tensor, and ϕ is the Brans-Dicke field by which the locally measured gravitational constant can be written as

$$G = \phi^{-1}\frac{2\omega+4}{2\omega+3} . \quad (2.4)$$

Dicke has pointed out [20] that the theory can also be expressed in another frame, the so-called Einstein frame, and in this frame, the equations become

$$R_{ab} - \tfrac{1}{2} g_{ab} R = 8\pi e^{-\Phi} \hat{T}_{ab} = \omega' (\nabla_a \Phi \nabla_b \Phi - \tfrac{1}{2} g_{ab} g^{cd} \nabla_c \Phi \nabla_d \Phi) , \quad (2.5)$$

$$\nabla_a \nabla^a \Phi = \frac{4\pi}{\omega'} e^{-2\Phi} \hat{T}^a_a , \quad (2.6)$$

and

$$\nabla_a \hat{T}^a_b = 2(\nabla_a \Phi) \hat{T}^a_b - \tfrac{1}{2} (\nabla_b \Phi) \hat{T}^a_a , \quad (2.7)$$

where $\omega' = \omega + \frac{3}{2}$, $\Phi = \ln(\phi)$, and $g_{ab} = \phi \hat{g}_{ab}$. R_{ab}, R, and ∇ are the Ricci tensor, Ricci scalar, and covariant derivative with respect to g_{ab}, respectively.

Here, in the Einstein frame, the equations are essentially the same as the Einstein equation with a scalar field Φ, while the equations in the Brans-Dicke frame are somewhat complicated because they include the second derivatives of ϕ in the right-hand side (RHS) of Eq. (2.1). Hence for convenience of numerical computation, we solve the equations in the Einstein frame.

We numerically treat the spherically symmetric dust collapse in the Brans-Dicke theory. In numerical calculation, we use the 3+1 formalism and choose the line element (i.e., the gauge condition) as

$$ds^2 = -\alpha^2 dt^2 + A^2 dr^2 + B^2 r^2 (d\theta^2 + \sin^2\theta \, d\varphi^2) . \quad (2.8)$$

As for the time coordinate, we adopt the maximal slicing condition, $K = 0$. Then, in the above gauge, $K = -\partial_t (AB^2)/AB^2$, so that AB^2 is constant with respect to the time t and depends only on the radial coordinate r.

The energy-momentum tensor of the dust fluid is written as

$$\hat{T}_{ab} = \hat{\rho} \hat{u}_a \hat{u}_b , \quad (2.9)$$

where $\hat{\rho}$ and $\hat{u}^a$ are the baryon mass density and the four-velocity in the Brans-Dicke frame. This means that $-\hat{u}^a \hat{u}_a$ does not become unity but ϕ in the Einstein frame. Furthermore, the equation for $\hat{\rho}$ does not become a flux conservative equation. Instead, it becomes

$$\nabla_a (\hat{\rho} \hat{u}^a) = 2(\nabla_a \Phi) \hat{\rho} \hat{u}^a . \quad (2.10)$$

Thus, we define $\rho = \hat{\rho} e^{-2\Phi}$. In this case the equation becomes the conservative form

$$\nabla_a (\rho \hat{u}^a) = 0 . \quad (2.11)$$

Taking into account these facts, we define the fluid variables as

$$\rho_h = \rho AB^2 (\alpha \hat{u}^0)^2, \quad S_r = \alpha AB^2 \rho \hat{u}^0 \hat{u}_r , \quad (2.12)$$

$$D = \alpha AB^2 \rho \hat{u}^0, \quad S^0 = D \hat{u}^0 , \quad V^r = \frac{\hat{u}_r e^{\Phi}}{\hat{u}^0 A^2} .$$

We also define the following quantities to guarantee the regularity at $r = 0$:

$$S_1 = S_r / r, \quad V_1 = V^r / r . \quad (2.13)$$

Then the equations of the dust become

$$\partial_t D + \frac{1}{r^2} (r^3 D V_1)_{,r} = 0 \quad (2.14)$$

and

$$\partial_t S_1 + \frac{1}{r^3} (r^4 S_1 V_1)_{,r} = -2 S^0 \alpha \alpha_{,y} e^{-\Phi} + 2 \frac{S_1^2 A_{,y}}{S^0 A^3} y e^{\Phi} + \frac{D^2}{S^0} \Phi_{,y} , \quad (2.15)$$

where $y = r^2$. S^0 becomes

$$S^0 = \frac{1}{\alpha} \sqrt{e^{\Phi} D^2 + e^{2\Phi} A^{-2} y S_1^2} . \quad (2.16)$$

The equation of the scalar field becomes

$$\partial_t \Phi = \frac{\alpha}{AB^2} \eta ,$$
$$\partial_t \eta = \frac{\alpha B^2}{2} \left\{ 4y \Phi_{,yy} + 6 \Phi_{,y} + 4y \Phi_{,y} \left(\frac{\alpha_{,y}}{\alpha} + 2 \frac{B_{,y}}{B} - \frac{A_{,y}}{A} \right) \right\} + \frac{4\pi}{\omega'} \frac{D^2}{S^0} . \quad (2.17)$$

To solve the metric and extrinsic curvature, we have several choices to treat the equations in the Brans-Dicke theory because they also have the constraint equations as well as the evolution equations. Here we adopt the following method: (1) As for the three-metric, we solve the evolution equation of A, so that B is obtained from $AB^2 = \psi^6(r) = \text{const}$, where ψ is fixed at the stage of the initial value equations (see below); (2) as for the extrinsic curvature $K^r_r (\equiv K_1)$, we solve the momentum constraint equation; (3) the Hamiltonian constraint is used to check the accuracy.

Then the basic equations become

$$\partial_t A = -\alpha K_1 A , \quad (2.18)$$

$$B = \psi^3 / \sqrt{A} , \quad (2.19)$$

$$4y \alpha_{,yy} + 6 \alpha_{,y} + 4y \alpha_{,y} \left(2 \frac{B_{,y}}{B} - \frac{A_{,y}}{A} \right) = 4\pi \alpha \left(\frac{A \rho_h e^{-\Phi}}{B^2} + \frac{A S_1 V_1 y}{\alpha B^2} \right) + \frac{3}{2} \alpha K_1^2 A^2 + \omega' \alpha \frac{\eta^2}{B^4} , \quad (2.20)$$

and

$$K_1 = r^{-3} B^{-3} \int_0^r dr \, r^4 A^{-1} B [8\pi S_1 - 2\omega' \eta \Phi_{,y}] . \quad (2.21)$$

The first equation is the evolution equation of A. The second and third equations are obtained from the maximal slicing condition $K = 0$. The fourth equation is obtained from the momentum constraint.

To obtain the initial condition, we must solve the Hamiltonian constraint. By virtue of the spherical symmetry, we can consider, without loss of generality, the conformally flat initial condition $A = B = \psi^2$. Then, in this case, the Hamiltonian constraint becomes

$$4y\psi_{,yy} + 6\psi_{,y} = -2\pi\frac{\rho_h e^{-\Phi}}{\psi} - \frac{3}{16}\psi^5 K_1^2 - \frac{\omega'}{8}[\eta^2\psi^{-7} + 4(\Phi_{,y})^2 y\psi] \ . \quad (2.22)$$

Before proceeding further, we briefly review the behavior of the metric in the wave zone [16]. Since metric quantities, α, A, and B, do not contain the wavelike component in the wave zone, in the Brans-Dicke frame (denoted by $d\hat{s}$), the line element in this zone becomes

$$d\hat{s}^2 = (1+\Phi)ds^2 \ , \quad (2.23)$$

where ds^2 is the component that does not contain the wave part and $|\Phi| \ll 1$. This means that, in the wave zone, we may regard Φ as just the SGW's. Therefore, to see SGW's in the wave zone, we have only to see the Brans-Dicke scalar field.

B. Numerical method and test of code

We solve the above equations by means of the finite difference method. In order to see the SGW's clearly, as for the partial derivatives of the scalar field, metric, and extrinsic curvature, such as $\partial_t A$ and $A_{,y}$, we use the second-order finite difference as follows:

$$\partial_t A^n = \frac{1}{\Delta t_n + \Delta t_{n-1}}\left\{\frac{\Delta t_{n-1}}{\Delta t_n}(A^{n+1} - A^n) + \frac{\Delta t_n}{\Delta t_{n-1}}(A^n - A^{n-1})\right\} , \quad (2.24)$$

$$A_{,y} = \frac{1}{y_{i+1} - y_i}\left\{\frac{y_i - y_{i-1}}{y_{i+1} - y_i}(A_{i+1} - A_i) + \frac{y_{i+1} - y_i}{y_i - y_{i-1}}(A_i - A_{i-1})\right\} ,$$

where A^n, Δt_n, and A_i, respectively, denote A at the nth time step, the time difference between the nth and the $(n+1)$th steps, and A at y_i. As for the fluid equation, we use the standard flux conservative method [21]. In numerical calculation, typically, we take 4000 grid points for $r_i(y_i)$, and the outer grid becomes about 1000 M. For one calculation it took about 10 h on a YHP 715-50 work station.

To see the accuracy of the numerical code, we perform several test problems. In Figs. 1(a) and 1(b), we compare the results for the Oppenheimer-Snyder (OS) collapse calculated by the numerical code and semianalytical method, respectively. Here, we call essentially the same method as that used by Petrich, Shapiro, and Teukolsky [22] the semianalytical method, although the present gauge condition is not the same as theirs. (Their spatial coordinate condition is the conformally flat gauge.) For the test problem, the initial radius for OS collapse is chosen as $r/M = 10$, where r is the coordinate radius in the present gauge. In Figs. 1(a) and 1(b), we show α and A at $t/M = 46.1$ and 57.3, respectively, as an example. Solid lines show the semianalytic solution, and the square symbols show the numerical results. These figures show

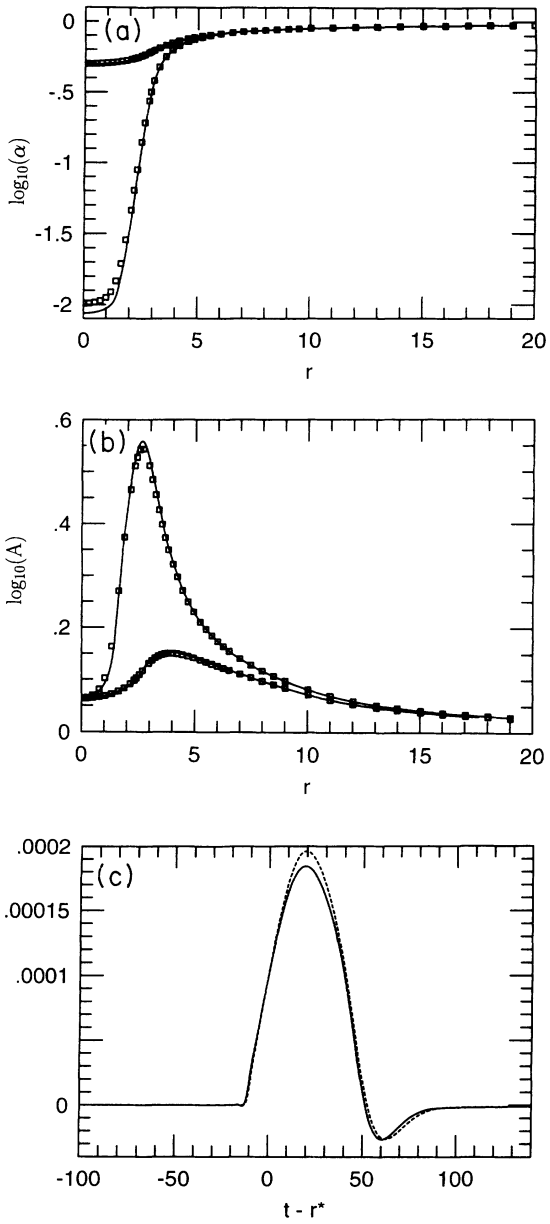

FIG. 1. (a) The lapse function α as a function of the coordinate radius on selected time slice $t/M = 46.1$ and 57.3 for Oppenheimer-Snyder collapse from $r/M = 10$. The solid line shows the results calculated by the semianalytical method, and square symbols denote those calculated by the numerical code. (b) The same as (a), but for A. (c) The scalar waves induced by a spherical dust shell, which initially rests at $r_s = 10M$ and falls into a Schwarzschild black hole. The solid and dashed lines show the results by the perturbation study and the numerical simulation, respectively.

that the present numerical method works well.

We also perform the comparison of wave forms of scalar waves calculated by the perturbation study around a Schwarzschild black hole and by numerical simulation. Here, the method of the perturbation study is essentially the same as the perturbation study of gravitational waves around a black hole. (See, for example, Ref. [26].) In Fig. 1(c), we show the numerical results of Φr at $r \sim 100\,M$ induced by a spherical dust shell, which initially rests at $r_S = 10\,M$, where r_S is the areal radius and falls into a Schwarzschild black hole. In this calculation, the mass of the dust shell is set as $\mu = M/10$, so that two results should agree within an accuracy of $\sim 10\%$. In numerical simulation, the black hole is expressed by the compact dust clump whose radius $R \sim 0.3\,M$ initially. In the figure, solid and dashed lines show the results by the perturbation study and the numerical simulation, respectively. It is found that both results agree very well. This also shows that the present numerical method works well.

III. NUMERICAL RESULTS

A. Initial conditions

As for the initial density configuration of the dust, $\rho_{h|t=0}$, we adopt

$$\rho_h = \rho_c[1 + \exp\{(y - y_1)/2y_2\}]^{-1} , \tag{3.1}$$

where ρ_c, y_1, and y_2 are constant free parameters. Since we treat the dust, we can freely scale the unit of mass. For convenience, we determine ρ_c to fix $M = 1$. Hence, the remaining free parameters are y_1 and y_2. In the case of $y_1 \gg y_2$, the distribution is almost homogeneous, while, in the case of $y_1 \ll y_2$, it becomes a Gaussian-type distribution. Here, we must be careful to give these parameters because, if we choose an inappropriate set of the parameters, the naked singularity due to the shell focusing [23] appears during numerical simulations and the simulation must be stopped before the SGW's propagate to the wave zone. Experimentally, we found that such a singularity seems to appear in the case of $y_1 \lesssim y_2$, so we adopt parameters satisfying $y_1 \geq y_2$.

Before we give the initial condition of Φ and η, we should note the following: In the initial data, there is no information about the equation of state for baryonic matters, although we treat $p = 0$ dust in the dynamical evolution. This means that we may consider our simulations as follows: For $t < 0$, the matter is almost under the equilibrium state (so $\eta = 0$), and, for $t \geq 0$, the pressure is reduced to zero and the collapse begins. Taking into account the above, we consider two types of initial conditions. We call them cases (A) and (B). As for case (A), we use the initial condition, $\Phi = \eta = 0$. We adopt case (A) just for simplicity, but we can regard it as the highly relativistic initial condition because it is consistent with $\hat{T}^a_a = -\rho(1 + \epsilon) + 3P = 0$, where ϵ is the internal energy per baryon mass. As for case (B), we adopt the more realistic initial condition. In realistic situations of stellar cores before collapse, the equation of state in the equilibrium state will be mainly determined by neutrino pressure [24]. In this case, the equation of state will become $p \sim \rho\epsilon/3$ and $\hat{T}^a_a$ becomes $-\rho$. To take into account this property, we calculate the initial condition of Φ from the following equation, which is obtained from Eq. (2.17) inserting $\partial_t\eta = \eta = 0$:

$$4y\Phi_{,yy} + 6\Phi_{,y} + 4y\Phi_{,y}\left(\frac{\alpha_{,y}}{\alpha} + 2\frac{B_{,y}}{B} - \frac{A_{,y}}{A}\right) = -\frac{4\pi A}{\omega' B^2}\rho_h \ . \tag{3.2}$$

Note that if we solve this equation, the asymptotic value of Φ becomes $\sim M/r\omega'$. In both cases, the momentum constraint is satisfied automatically ($K_1 = 0$) and we have only to solve the Hamiltonian constraint to obtain the initial condition.

B. Numerical results

We have performed numerical computations for a variety of parametrs y_1, y_2, and ω' for both cases (A) and (B). We show the parameters as well as the density at the center ρ_c for selected models in Table I. Since the unit of the density is $6.17 \times 10^{17}\ \mathrm{g\,cm^{-3}}(M_\odot/M)^2$, the central densities in the initial conditions are $\sim 10^{11}$–$10^{14}\ \mathrm{g\,cm^{-3}}$ for $M = 1M_\odot$–$10M_\odot$.

First, to see the effects of ω' on the waveforms of emitted SGW's, we compare the wave forms of models (A1)–(A3) in Fig. 2. The vertical axis corresponds to $\Phi(\omega'/500)$ at the numerical boundary. The solid line, dot-dashed line, and dashed line show the waveforms of models (A1)–(A3). We note that the unit of the time t is $4.93\times10^{-5}(M/10M_\odot)$ sec. Amplitudes of SGW's are shown in units of $h = \Phi(R/M)$, where R is the areal radius from the detector to the source. Hence, the amplitude at the detector becomes

$$\Phi \sim 10^{-22}\left(\frac{h}{0.002}\right)\left(\frac{M}{10M_\odot}\right)\left(\frac{10\ \mathrm{Mpc}}{R}\right) . \tag{3.3}$$

TABLE I. Initial conditions for models (A1)–(A8) and (B1)–(B4).

Model	ω'	$\sqrt{y_1}$	$\sqrt{y_2}$	ρ_c
(A1)	500	15	0.4	7.4×10^{-5}
(A2)	50	15	0.4	7.4×10^{-5}
(A3)	5	15	0.4	7.4×10^{-5}
(A4)	500	15	6	6.4×10^{-5}
(A5)	500	30	0.4	9.0×10^{-6}
(A6)	500	10	0.4	2.6×10^{-4}
(A7)	500	10	4	2.2×10^{-4}
(A8)	500	5	0.4	2.1×10^{-3}
(B1)	500	30	0.4	9.0×10^{-6}
(B2)	500	15	0.4	7.4×10^{-5}
(B3)	500	10	0.4	2.5×10^{-4}
(B4)	500	5	0.4	2.1×10^{-3}

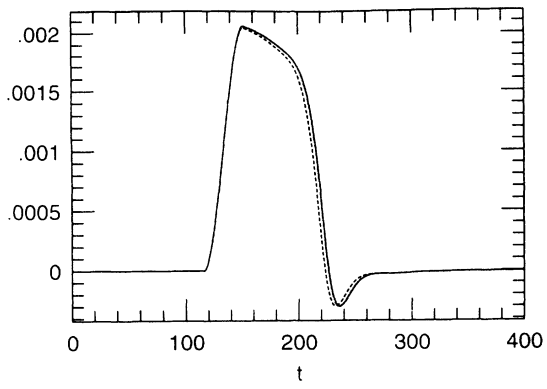

FIG. 2. Waveforms of the scalar wave observed in the wave zone are shown for models (A1)–(A3). The amplitudes for models (A2) and (A3) are written on scales of 1–10 and 1–100, respectively. The solid line, the dot-dashed line, and dotted line show for models (A1)–(A3), respectively. Lines for models (A1) and (A2) overlap each other.

From Fig. 2, it is found that shapes of the waveforms are almost the same, so that the ratio of the amplitudes is the same as the ratio of ω'; the scalar fields are linearly scaled with ω'. This means that the Brans-Dicke scalar fields behave like linear perturbations and does not affect the dynamics of the matter field and the metric so much, even in the case of $\omega' = 5$. (This is consistent with the simulations performed by Matsuda and Nariai [25] 20 years ago.) In fact, the maximum value of Φ is $\sim 10^{-3}$ for $\omega' = 500$, and ~ 0.1 even for $\omega' = 5$. Therefore, we may regard the scalar field as the linear perturbation for $\omega' \geq 5$, and we can linearly extrapolate the results obtained in the present calculations to the cases of large ω'. Taking into account this fact, hereafter, we only show the numerical results for the case of $\omega' = 500$.

In Fig. 3, we show the various waveforms for models (A4)–(A8) and (B1)–(B4). Since the initial values of h for case (B) are approximatley ~ 0.002, the amplitude of the wave for (A) and (B) are different before the oscillation of the wave begins, but the difference between (A) and (B) is only their initial values. Since the final products are the black holes in all models, h becomes 0 at[1] $t \to \infty$[19] and the maximum $|\nabla h|$ becomes ~ 0.002 irrespective of the models. Therefore, we can expect that irrespective of the initial condition, the maximum amplitude $\Phi_{\max}$ of SGW's at the wave zone becomes

$$\Phi_{\max} \sim 10^{-22}\left(\frac{M}{10M_\odot}\right)\left(\frac{10\ \mathrm{Mpc}}{R}\right)\left(\frac{500}{\omega}\right) . \quad (3.4)$$

As for the waveforms shown in Fig. 3, we can see the following features.

(1) For the case (A), as the initial configuration of dust is more compact (y_1 is smaller) or less condensed (y_2 is larger), the wave rises more sharply and the wavelength becomes shorter. Also for case (B), as the initial configuration of dust is more compact (y_1 is smaller), the wave descends more sharply.

(2) All the models have the same waveforms during their damping.

Property (1) reflects the motion of the dust, while property (2) seems to reflect a feature of the space-time; that is, we see the quasinormal mode (QNM) of the black hole. To confirm that these are the QNM's, we show the various results of the perturbation study on a Schwarzschild space-time. In Fig. 4, we show the scalar waves induced by spherical dust shells, which initially rest at $r_s/M = 5, 10, 20$. From the figure, we can see the same damping waveforms as those in Fig. 3.

In Fig. 5, we show the Fourier spectrum for models (A1) and (A4)–(A8). Horizontal lines show that the $\log_{10} f$, and the unit of the frequency f becomes $2.03\times10^4(10M_\odot/M)$ Hz. The Fourier spectrum is defined as

$$h_f = \int_0^{t_{\max}} h(t)\exp(2\pi i f t)dt , \quad (3.5)$$

and in figures, we plot $f|h_f|/0.002 \equiv H_f$. Note that the unit of H_f is

$$10^{-22}\left(\frac{M}{10M_\odot}\right)\left(\frac{10\ \mathrm{Mpc}}{R}\right)\left(\frac{500}{\omega'}\right) , \quad (3.6)$$

and it is the quantity to be compared with the root mean square (rms) noise ($h_{\mathrm{rms}} = [fS(f)]^{1/2}$) at each frequency of the detector [1,2]. From Fig. 5, it is found that H_f has the following features: (1) There is a characteristic frequency f_c. Below f_c, H_f damps linearly and irrespective of the model, $H_f \sim 10^{-0.5} \simeq 0.3$ at $f = f_c$; (2) f_c is approximately proportional to $\sqrt{\rho_c}$; (3) for $f \geq f_c$, there are a few peaks in the spectrums, and the value of some peaks as large as that at $f = f_c$, i.e., $0.2 \lesssim H_f \lesssim 0.3$.

As for feature (3), the peak frequencies are 200–$400(10M_\odot/M)$ Hz, and they are not so different for each model. This means that they reflect the QNM of the black hole because the estimation of the frequency f_{QNM} of the QNM by the WKB approximation [27] shows

$$f_{\mathrm{QNM}} \lesssim 500(M/10M_\odot)\ \mathrm{Hz} . \quad (3.7)$$

Hence, in the case of the neutron-star formation, QNM's will have different frequencies (see below). On the other hand, features (1) and (2) mean that although the maximum amplitude is independent of the initial condition, the characteristic frequency f_c of the Fourier spectrum is determined by the initial configuration. This will reflect that the scalar field is driven out of the black hole, and its time scale depends on the motion of the matter, i.e., the formation process of the black hole. A remarkable feature for case (A) is that H_f at $f = f_c$ is always greater than that at the frequency of the QNM. This is because the waveform is not dominated by the QNM contrary to the case of + and × mode of gravitational waves [28].

[1]In the case of the neutron-star formation, the results will be different because h will become a finite value. See the discussion below.

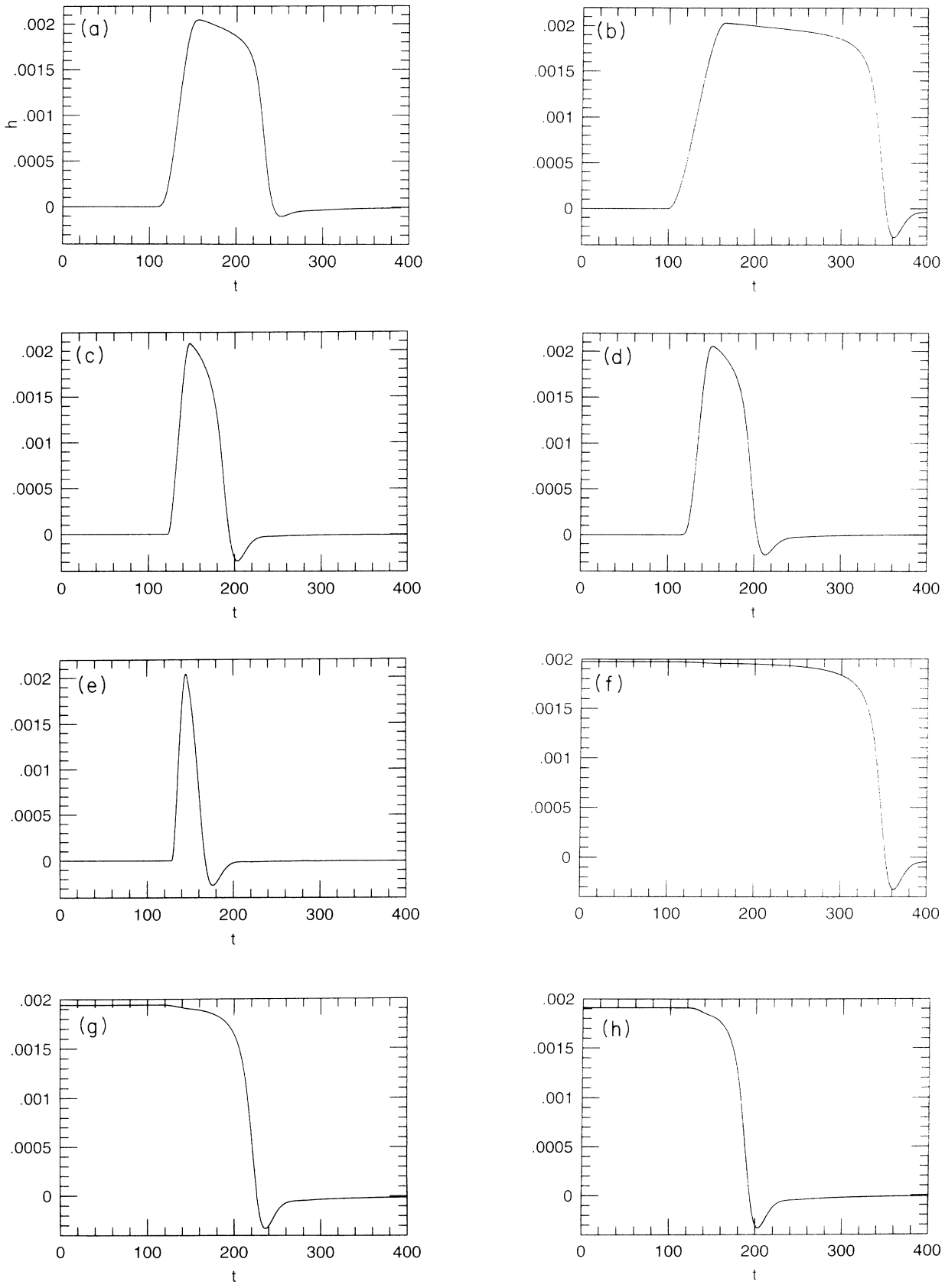

FIG. 3. Waveforms of the scalar wave observed in the wave zone are shown for models (A4)–(A8) and (B1)–(B4). The unit of time is $4.93\times10^{-5}(M/10M_{\odot})$ second. (a)–(e) and (f)–(i) correspond to that for models (A4)–(A8) and (B1)–(B4), respectively.

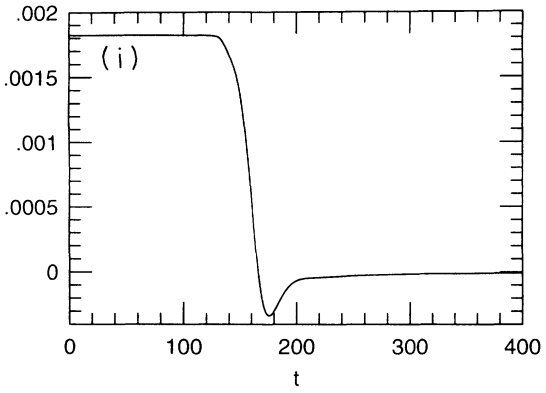

FIG. 3. (*Continued*).

This is just the useful property for the detection problem, since advanced LIGO [1] has good sensitivity in the frequency band $\sim$ 50–300 Hz. In this case, f_c becomes 50–400$(10M_\odot/M)$ Hz, and the maximum amplitude becomes

$$3\times10^{-23}\left(\frac{M}{10M_\odot}\right)\left(\frac{10\text{ Mpc}}{R}\right)\left(\frac{500}{\omega'}\right) . \tag{3.8}$$

Advanced LIGO [1] has the ability to detect the signal of the amplitude 10^{-23} at $\sim$ 70 Hz, and 3×10^{-22} at 30–200 Hz, so that the characteristic frequency of the SGW by the gravitational collapse seems almost equal to the most sensitive frequency for LIGO.

To consider the Fourier spectrum for the case (B1)–(B4) we must be careful because the waveforms of them are similar to the step function, and the Fourier spectrum will not become the same if we change the interval of integration time (i.e., the window function). Since in the realistic situation we consider the Fourier spectrum of $\tilde{h}(t)=h(t)-h(-\infty)$, not $h(t)$, hereafter we treat the Fourier transformation of $\tilde{h}$. First we consider the Fourier spectrum without the window function, which is written as

$$h_f=\int_0^T\tilde{h}(t)\exp(2\pi ift)dt , \tag{3.9}$$

where we take $T\gg f_{\rm QNM}^{-1}, f_c$. Then the integral near $f\sim f_{\rm QNM}, f_c$ becomes

$$h_f\simeq\tilde{h}(\infty)\frac{\exp(2\pi ifT)-\exp(2\pi ift_i)}{2\pi if} , \tag{3.10}$$

where t_i is the time when the wave begins to rise. Taking into account $T\gg t_i$, H_f becomes

$$0.002H_f\simeq\frac{|h(\infty)|}{\pi}|\sin(\pi fT)| . \tag{3.11}$$

Hence the spectrum does not have the characteristic frequency around $f_{\rm QNM}$, and it seems difficult to confirm whether the wave comes or not because we cannot find even the QNM.

Therefore we should consider the Fourier spectrum with window functions. We use the square-type window function [21], and then the Fourier spectrum becomes

$$h_f\equiv\int_0^{t_f}\tilde{h}(t)\exp(2\pi ift)dt , \tag{3.12}$$

where t_f is a cutoff time. As t_f, we choose the time when the SGW is regarded to stop oscillating. We should note that if we choose the larger t_f, the spurious peaks of the Fourier spectrum appear. This suggests that to confirm the detection of SGW's in realistic detections, we need an appropriate choice of window width $\sim 5(M/10M_\odot)$ ms. In Figs. 6(a)–6(d), we show the results of H_f when we choose $t_f/M=410,270,240,220$, respectively. In this case, the shapes of the Fourier spectrum are almost the same and have a peak around $f\sim10^{-2}$, so that we may consider that we extract the frequency of the QNM. In contrast, we cannot find the difference of the spectrum due to the initial condition or ρ_c, which is found in case (A). Therefore, the Fourier spectrum of SGW's emitted in the realistic black-hole formation may be dominated by the QNM. Nevertheless the maximum amplitude is also

$$3\times10^{-23}\left(\frac{M}{10M_\odot}\right)\left(\frac{10\text{ Mpc}}{R}\right)\left(\frac{500}{\omega'}\right) , \tag{3.13}$$

and the peak frequency is

$$\sim200\left(\frac{10M_\odot}{M}\right)\text{ Hz} . \tag{3.14}$$

Hence SN in the Virgo cluster seems to be an adequate target for the advanced LIGO.

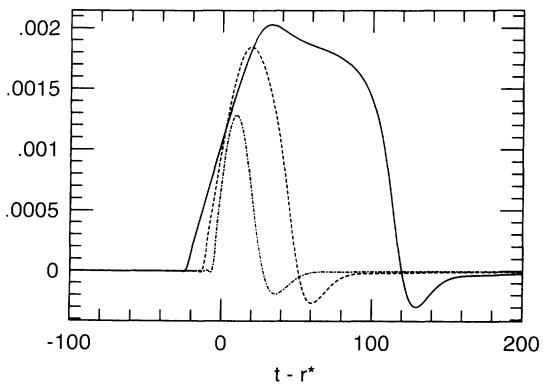

FIG. 4. Waveforms of the scalar wave induced by spherical dust shells which are initially at rest $r_s/M=5$ (dot-dashed line), 10 (dashed line), and 20 (solid line) and falls into a Schwarzschild black hole of mass $M=1$. A vertical axis shows $\Phi r(\mu/M)$. We can see the same characteristic damping waveforms in all cases although the total waveforms are not the same.

Although in case (B) the possibility of detecting SGW's depends on the window function [i.e., we need an appropriate window width $\sim 5(M/M_\odot)$ ms], we proceed with discussions assuming that the appropriate choice of the window function is achieved. Until now we have considered SGW's from the black-hole formation and seen that they have an amplitude and a frequency to be detected by the advanced LIGO. However, we must be careful to conclude that they are always emitted with such amplitude and frequency becuase in realistic SN's, a neutron star will be formed in most cases. We may overestimate the amplitude of SGW's using our results because in the case of black-hole formation, matter moves more rapidly in the strong gravitational field compared with neutron-star formation. For example, let us consider the + and × modes. From the quadrupole formula, the amplitudes of them are written as

$$h \sim \frac{Mv^2}{R}, \tag{3.15}$$

where v denotes the characteristic speed of the matter in the system. Hence, compared with the case of black-hole formation, h will be suppressed in the case of neutron-

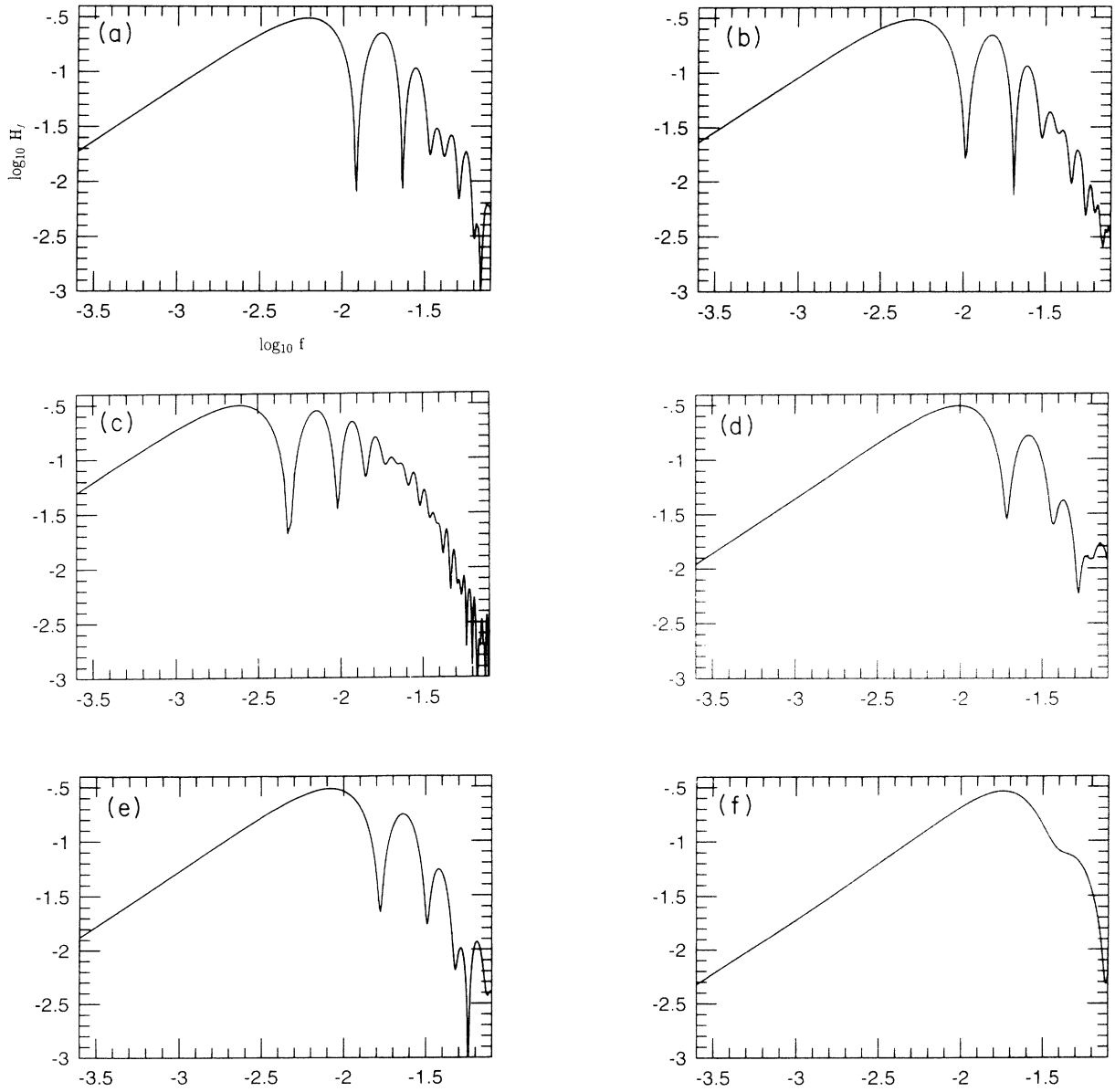

FIG. 5. Fourier spectrum of the SGW's for models (A1), (A4)–(A8). The unit of the frequency is $2.03\times10^4(10M_\odot/M)$ Hz. (a)–(f) correspond to that for models (A1), (A4)–(A8). The horizontal line and the vertical line show $\log_{10}f$ and $\log_{10}(fh_f/0.002)$, respectively. So that, in the horizontal axis, $-2(-3)$ corresponds to $203(20.3)(10M_\odot/M)$ Hz and, in the vertical axis, -1 (-2) corresponds to 10^{-23} (10^{-24}).

star formation. However, we think that the amplitude of SGW's in the case of neutron-star formation is not very different from that in the case of black-hole formation because of the following reason: We can evaluate the amplitude of the scalar field in the static space-time by a simple order estimate using a quadrupole-like formula, which may be called a monopole formula:

$$\Phi \sim \frac{1}{\omega' R} \int \hat{T}\, dV \ . \tag{3.16}$$

In the case of stellar core collapse, $\hat{T}$ will change from $\sim -\rho$ for the precollapse star with $P \sim \rho\epsilon/3 \ll \rho$ to $\sim -\rho(1+\epsilon) + 3P \sim$ several $\times \rho/10$ for the protoneutron star with $P \sim \rho\epsilon \lesssim \rho$ [24]. This means Φ changes from $M/R\omega'$ to several $\times M/10R\omega'$. Therefore $\Delta\Phi$ is expected to become

$$\Delta\Phi \sim \text{several} \times \frac{M}{10R\omega} \sim 10^{-23}\left(\frac{M}{1.4M_\odot}\right)\left(\frac{10\ \text{Mpc}}{R}\right)\left(\frac{500}{\omega}\right) . \tag{3.17}$$

Thus even in the case of the neutron-star formation, the maximum amplitude of SGW's will become $\sim 10^{-23}(M/1.4M_\odot)(10\ M_{\rm pc}/R)(500/\omega)$ irrespective of the initial condition and the formation process (e.g., v).

Although the maximum amplitude is almost the same, irrespective of the final products and the initial conditions, the characteristic frequency will be different. From the present calculations, it is found that the characteristic frequency f_c is determined by the time scale in which the configuration of the scalar field changes or the frequency of the QNM. In the case of the neutron-star formation, the frequency of the QNM is not clear, but is expected to become [29]

$$f_{\rm QNM} \lesssim \frac{1}{4}\sqrt{\rho \rm NS} \sim 1\ \text{kHz}\left(\frac{\rho_{\rm NS}}{2.8\times 10^{14}\ \text{g cm}^{-3}}\right)^{1/2} . \tag{3.18}$$

In case (A), extrapolating the numerical results, f_c becomes

$$f_c \sim 1.5\sqrt{\rho_c} \sim 40\ \text{Hz}\left(\frac{\rho_c}{10^{10}\ \text{g cm}^{-3}}\right)^{1/2} . \tag{3.19}$$

Hence, the frequency will become $40 \lesssim f \lesssim 1000$ Hz at which LIGO has good sensitivity. Thus, we can conclude that if the Brans-Dicke theory is correct and ω is less than a few thousands, SGW's from the SN in the Virgo cluster may be detected by advanced LIGO. Furthermore, if we happen to find a SN in our Galaxy, we can detect SGW's from it even though ω is as large as $\sim 10^6$. On the other hand, when nothing is detected by LIGO even if we find that a SN occurs in the Virgo cluster (or our Galaxy) by means of optical observation (or neutrino observation), we may say that ω is larger than a few thousands (or 10^6).

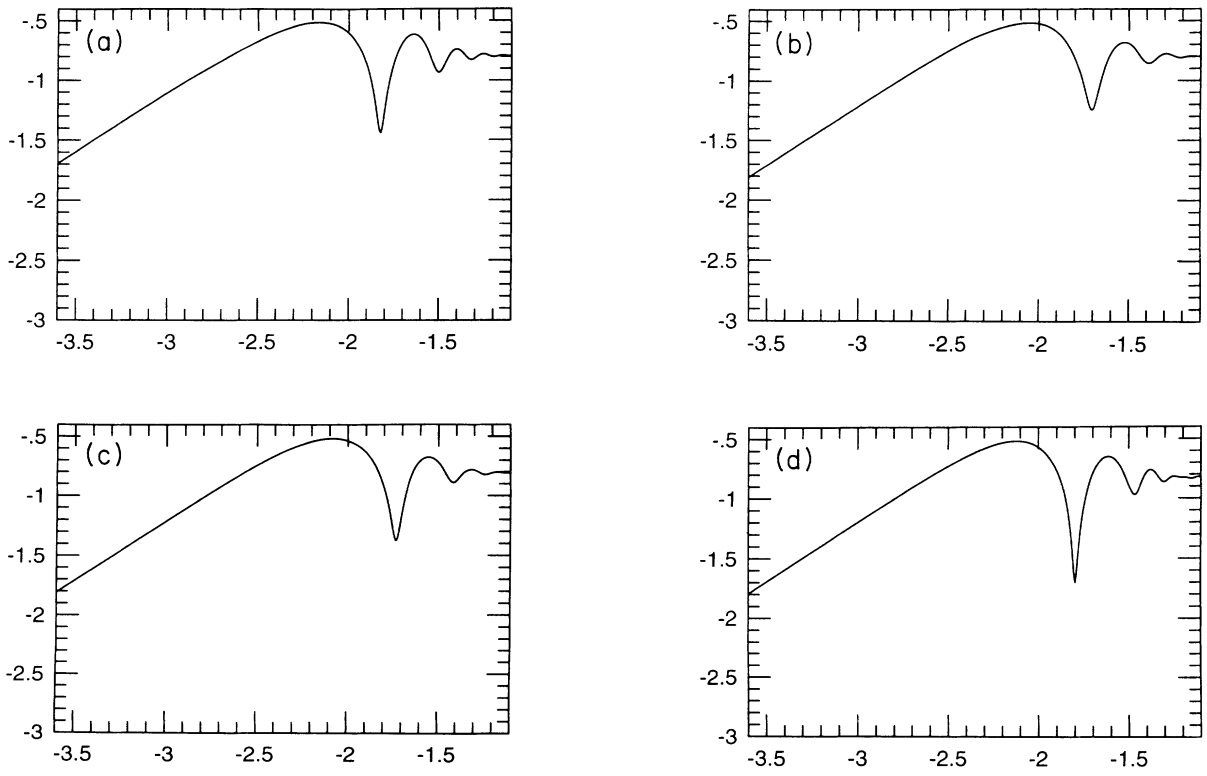

FIG. 6. The Fourier spectrum with the window function for model (B1)–(B4). The units are the same as for Fig. 5.

C. Detection of SGW's

In the above, our discussion assumed that the laser interferometric detector has the ability to detect SGW's, whereas it is a nontrivial problem. Thus, we here briefly show it as possible in reality.

In the wave zone composed of SGW's, the line element can be written as

$$d\hat{s}^2 = (1+\Phi)(-dt^2 + dx^2 + dy^2 + dz^2) \ . \tag{3.20}$$

This is the conformally flat space-time in which the null structure is completely the same as the Minkowski space-time, so that the laser (light) does not change their pass and the phase shift does not occur, by SGW's, as long as the laser goes along a null geodesic. Hence, it seems to be impossible to detect SGW's by the laser interferometric detector. However, this is not the case. We should note that the laser is reflected by the mirror again and again in the detector and the pass of the laser changes. If the mirror is not influenced by SGW's and rests, there is no signal in the detector, since the laser goes along the null geodesic effectively. However, if the mirror is perturbed by SGW's, the phase difference is caused and the interferometric detector can detect SGW's. As will be shown below, in reality it happens.

When the SGW comes from a very distant source, it can be approximated as a plane wave at the detector. Hence, we assume that the SGW Φ is a function of t-z and, in this case, the geodesic equation of a mirror becomes

$$\frac{d}{d\tau}\left[(1+\Phi)\frac{dt}{d\tau}\right] = \frac{1}{2}\frac{\partial_t(1+\Phi)}{1+\Phi} \ , \tag{3.21}$$

$$\frac{d}{d\tau}\left[(1+\Phi)\frac{dx}{d\tau}\right] = 0 = \frac{d}{d\tau}\left[(1+\Phi)\frac{dy}{d\tau}\right] \ , \tag{3.22}$$

$$\frac{d}{d\tau}\left[(1+\Phi)\frac{dz}{d\tau}\right] = -\frac{1}{2}\frac{\partial_z(1+\Phi)}{1+\Phi} \ , \tag{3.23}$$

where τ is the proper time of the mirror and in order to derive the above equations we have used the relation

$$\left(\frac{dt}{d\tau}\right)^2 - \left(\frac{dx}{d\tau}\right)^2 - \left(\frac{dy}{d\tau}\right)^2 - \left(\frac{dz}{d\tau}\right)^2 = \frac{1}{1+\Phi} \ . \tag{3.24}$$

Equation (3.22) is immediately integrated and we obtain

$$\begin{aligned}(1+\Phi)\frac{dx}{d\tau} &= P_x = \text{const} \ , \\ (1+\Phi)\frac{dy}{d\tau} &= P_y = \text{const} \ .\end{aligned} \tag{3.25}$$

Since we assume that the mirror is at rest initially, P_x and P_y should vanish. This means that the motion of the mirror within the x-y plane does not occur even if the SGW $\Phi(t\text{-}z)$ arrives at the mirror.

On the other hand, the SGW causes a nontrivial motion of the mirror in the z direction. Here we introduce the retarded and advanced time coordinates (u, v) to make the equations simple:

$$u = t - z \quad \text{and} \quad v = t + z \ . \tag{3.26}$$

From Eqs. (3.21) and (3.23), we obtain

$$\frac{d}{d\tau}\left([1+\Phi(u)]\frac{du}{d\tau}\right) = \frac{\partial_v \Phi(u)}{1+\Phi(u)} = 0 \ . \tag{3.27}$$

Then we get

$$\frac{du}{d\tau} = \frac{a}{1+\Phi(u)} \ , \tag{3.28}$$

where a is an integration constant. From Eqs. (3.24) and (3.28), we find

$$\frac{dv}{d\tau} = \frac{1}{a} \tag{3.29}$$

and

$$\tau = av + b \ , \tag{3.30}$$

where b is an integration constant, which corresponds merely to the advanced time coordinate translation, and, hence, without loss of generality we will take it to be zero. In order to see the meaning of the other integration constant a, we write down the equation for z from Eqs. (3.28) and (3.29) as

$$\frac{dz}{d\tau} = \frac{1}{2a}\left(1 - \frac{a^2}{1+\Phi}\right) \ . \tag{3.31}$$

Before the SGW arrives at the mirror, i.e., $\Phi = 0$, the above equation becomes

$$\frac{dz}{d\tau} = \frac{1}{a}(1-a^2) \ . \tag{3.32}$$

This is just the initial velocity of the mirror, so we will choose $a = 1$ because the mirror initially rests.

Now we can find the motion of the mirror in the z direction by integrating Eq. (3.28) as

$$\begin{aligned} z = \tfrac{1}{2}(v-u) &= \tfrac{1}{2}\left(\int [1+\Phi(u)]du - u\right) \\ &= z_0 + \tfrac{1}{2}\int_{-\infty}^{t-x} \Phi(u)du \ , \end{aligned} \tag{3.33}$$

where z_0 is the initial location of the mirror and we have used the fact $\tau = v$. Then assuming $\Phi \ll 1$, the displacement of the mirror in the z direction is given by

$$\Delta z = z - z_0 = \frac{1}{2}\int_{-\infty}^{t-z_0-\Delta z} \Phi(u)du \simeq \frac{1}{2}\int_{-\infty}^{t-z_0} \Phi(u)du \ . \tag{3.34}$$

As shown above, the mirrors move only in the propagation direction z of the waves. This means that in the case that the detector lies on the x-y plane, the sensitivity of the detector is zero because the arm length of the laser interferometer does not change even if the SGW comes. However, the sensitivity of the detector to SGW's is not zero in the other cases because the arm length of the detector must be changed. The change of arm length means that the pass of the laser is also changed, so that the laser interferometer can measure the change, i.e., detect SGW's. (This also explains why the noise level of the laser interferometer to + and × modes of gravitational waves is roughly the same as that of the scalar mode.)

The antenna pattern of the laser interferometric detector is proportional to

$$[\mathbf{n}\cdot\mathbf{m}_1 - \mathbf{n}\cdot\mathbf{m}_2] = \sin\theta_s\sqrt{1-\sin 2\varphi_s} \ , \tag{3.35}$$

where $\mathbf{m}_1$ and $\mathbf{m}_2$ are the directions of the two arms of the detector and are assumed to be $\mathbf{m}_1 = (1,0,0)$ and $\mathbf{m}_2 = (0,1,0)$. $\mathbf{n} = (\theta_s, \varphi_s)$ describes the incoming direction of the wave to the detector [2]. Equation (3.35) means that if one of the arms of the detector agrees with the incoming direction of SGW, the sensitivity becomes maximum. In this case, the phase difference $\Delta\chi$ at the maximum displacement of the mirror is given by

$$\Delta\chi = \frac{2\pi\Delta z}{\lambda} \simeq \frac{\Omega}{2}\int_{-\infty}^{t-z_0} \Phi(u)du \ , \tag{3.36}$$

where λ and Ω are the wavelength and the angular frequency of the laser, respectively. Thus SGW's can be detected by the laser interferometric detectors.

It should be noted that the most sensitive directions of the detectors for the SGW's are perpendicular to those for + and × modes, i.e., their antenna patterns are different from those of SGW's. This means that if there exist four detectors and there are no modes except for the scalar, +, and × modes, we can distinguish the SGW's from the other two modes as well as we can determine the direction of the source.

IV. FATE OF COLLAPSED OBJECTS

To investigate whether or not the final fate of a collapsing object is a black hole, we investigated whether or not the apparent horizon [30] is formed in the numerical simulation. In this section, we briefly show the results.

In the gauge condition adopted in the present calculations, the location of the apparent horizon is obtained from

$$q(r) = K_1 + \frac{2}{A}\left(\frac{1}{r} + \frac{B_{,r}}{B}\right) = 0 \ . \tag{4.1}$$

In numerical simulations, we determine the location of the apparent horizon, $r = r_i$, from the condition

$$q(r_i)q(r_{i+1}) < 0 \ . \tag{4.2}$$

In all the models, we find that the apparent horizon was formed and these results strongly suggest that the black hole was formed. To make sure that those are the apparent horizon around the Schwarzschild black holes, we also calculate their area (S) from

$$S/M^2 = 4\pi B^2 r^2 \ . \tag{4.3}$$

We find that in all calculations S/M^2 becomes $\lesssim 16\pi$, where 16π is the area of the event horizon of the Schwarzschild black hole.

To see the final configuration of the scalar field, in Fig. 7 we show the time evolution of the scalar configuration for model (A2) as an example. We do not intend to show figures for other models because the results in the other calculations are essentially the same as that for model (A2). In Fig. 7, we show the configuration of the scalar field at $t/M = 136$ and 370, at which the loci of the apparent horizon are $r/M = 5.4$ and 9.5, respectively. It is found that outside the apparent horizon the value of the scalar field tends to vanish after the wave packet passes through this region, while it is not constant inside the apparent horizon. This also supports our conclusion, which states that the final products are the static Schwarzschild space-time.

We also performed simulations with the same ω' and same initial configuration of ρ_h as model (A2), but with a large initial value of Φ:

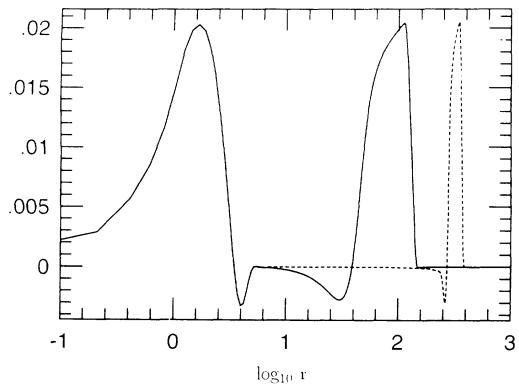

FIG. 7. Configurations of the scalar field as a function of $\log_{10} r \equiv z$ for model (A2) are shown for $t/M = 136$ and 370. A vertical axis shows $\Phi(r/M)$. Solid and dashed lines show the configuration for $t/M = 136$ and 370, respectively. Note that loci of the apparent horizon are $z = 0.73$ and 0.98 for $t/M = 136$ and 370, respectively.

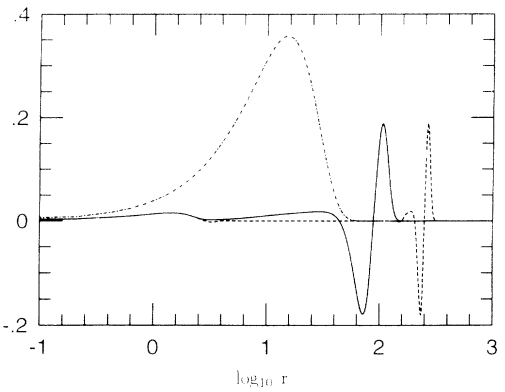

FIG. 8. The same as in Fig. 7, but for model (A2′). Dash-dotted, solid, and dashed lines show for $t/M = 2.3$, 74, and 257, respectively. Note that loci of the apparent horizon are $z = 0.44$ and 0.84 for $t/M = 74$ and 257, respectively.

$$\Phi = \Phi_c \exp\left(-\frac{y}{2y_1}\right) , \qquad \eta = 0 . \tag{4.4}$$

In Fig. 8, we show the numerical result of the time evolution of Φ for $\Phi_c = 4 \times 10^{-2} \gg M/(\omega' \sqrt{y_1})$ (i.e., an unrealistically large value) as an example. [We call this model (A2′).] Here, we choose the amplitude of the dust ρ_c in order that $M = 1$ and, as a result, 20% of the total mass M comes from the energy of the Brans-Dicke field. From Fig. 8, we find that Φ seems to be static at the late stage. It is also found that about 20% of the total energy M propagates as SGW's and the area of the apparent horizon approaches $\sim 4\pi(2 \times 0.8M)^2$. This means that most of the Brans-Dicke field merely propagate away in the gravitational collapse and do not affect the final fate very much. Thus, we may conclude that the final products after the spherically symmetric gravitational collapse in the Brand-Dicke theory are the Schwarzschild black holes, not the naked singularities [19].

V. SUMMARY

In this paper, we have considered the spherically symmetric gravitational collapse in the Brans-Dicke theory to see the feature of the emitted SGW's as well as the fate of the collapsed objects. We obtain results as follows.

(1) In realistic situations (i.e., for realistic values of ρ_c, y_1, and Φ_c), the scalar field does not affect the dynamics of the gravitational collapse for $\omega' \geq 5$. This is made certain by investigating the total-energy flux, which is emitted for less than 1% of the mass of the system. This ensures that we treat the Brans-Dicke field as a linear perturbation in the case of $\omega \geq 500$.

(2) In the case of black-hole formation, irrespective of initial conditions, the maximum amplitude of SGW's seems to become

$$\Phi \sim 10^{-22}\left(\frac{500}{\omega}\right)\left(\frac{M}{10M_\odot}\right)\left(\frac{10\ M_{\rm pc}}{R}\right) . \tag{5.1}$$

While the characteristic frequency f_c depends either on the QNM of the black hole, $f \sim 200$–$400M/10M_\odot$ Hz, or on the initial condition, in which f_c is approximately proportional to $\sqrt{\rho_c}$, where ρ_c is the density when the collapse to black hole begins, the characteristic amplitude becomes

$$\Phi_f f \sim 3 \times 10^{-23}\left(\frac{500}{\omega}\right)\left(\frac{M}{10M_\odot}\right)\left(\frac{10\ M_{\rm pc}}{R}\right) . \tag{5.2}$$

Using the results of the present calculation, we can roughly estimate that in the realistic gravitational collapse and the subsequent neutron star formation, f_c becomes

$$f_c \sim 40 - 1000 \text{ Hz} , \tag{5.3}$$

and its amplitude will be

$$\Phi_f f \sim 10^{-23}\left(\frac{500}{\omega}\right)\left(\frac{M}{1.4M_\odot}\right)\left(\frac{10\ M_{\rm pc}}{R}\right) . \tag{5.4}$$

These mean that advanced LIGO may detect SGW's from a SN at the Virgo cluster if ω is less than a few thousand, and, if we *happen* to find a SN in our Galaxy, we can detect SGW's *even though* ω *is as large as* $\sim 10^6$.

(3) The final products of the collapsed objects are Schwarzschild black holes, and outside the apparent horizon, the scalar field tends to become constant. This supports the cosmic censorship conjecture, which states that the final product of the gravitational collapse of nonrotating matter is a Schwarzschild black hole, and outisde the horizon scalar field converges to a constant.

In particular, result (2) is interesting in the light of the current resurgence of the scalar-tensor theories as either the inflationary scenario or the dilaton gravity predicted by the superstring theory. These theories predict the scalar-tensor theories, so that if we detect SGW's, not only will we know the correct theory of gravitation, but also we will obtain a clue about the very early Universe.

Although we did not mention it in this paper, the detection of gravitational waves from coalescing black-hole–neutron-star binaries or binary neutron stars of large mass ratio by laser interferometric detector can also be used as a test of the theory of gravities. As mentioned in Sec. I, the back reaction to the binaries of gravitational waves are different in each metric theory, so the evolution of them are different in each theory. Comparing the Einstein theory with the Brans-Dicke theory with $\omega = 500$, as an example, the difference of the accumulated cycles becomes about 3 in the case of $10M_\odot$–$1.4M_\odot$ black-hole–neutron-star binary [14], which we will be able to measure using the matched filter technique [3].

Thus, the observation of gravitational waves have a possibility of investigating the *last three minutes* of coalescing compact binary as well as the *first three minutes* of the Universe. Hence, detailed studies of the gravitational collapse and coalescing compact binary in the various scalar-tensor theories will be needed before the gravitational astronomy starts.

ACKNOWLEDGMENTS

We thank H. Ishihara, M. Sasaski, H. Tagoshi, and T. Tanaka for useful comments and discussions. K. N. is also grateful to H. Sato for his encouragement. This work was partly supported by a Grant-in-Aid Scientific Research on Priority Area of the Ministry of Education, Science and Culture, No. 04234104.

[1] R. E. Vogt, in *Sixth Marcel Grossmann Meeting on General Relativity*, Proceedings, Kyoto, Japan, 1991, edited by H. Sato and T. Nakamura (World Scientific, Singapore, 1991), p. 244; A. Abramovici *et al.*, Science **256**, 325 (1992); K. S. Thorne, in *Proceedings of the Eighth Nishinomiya Symposium on Relativistic Astrophysics*, Nishinomiya, Japan, 1993, edited by M. Sasaki (Universal Academy, Nishinomiya, 1993).

[2] K. S. Thorne, in *300 Years of Gravitation*, edited by S. W. Hawking and W. Israel (Cambridge University Press, Cambridge, England, 1987).

[3] C. Cutler *et al.*, Phys. Rev. Lett. **70**, 2984 (1993).

[4] L. E. Kidder, C. M. Will, and A. G. Wiseman, Phys. Rev. D **47**, R4183 (1993); M. Shibata, *ibid.* **48**, 663 (1993).

[5] C. Cutler and E. E. Flanagan, Phys. Rev. D **49**, 2658 (1994).

[6] M. Shibata, Prog. Theor. Phys. **90**, 595 (1993); T. A. Apostolatos, C. Cutler, G. J. Sussman, and K. S. Thorne (unpublished).

[7] A. Krolak and B. F. Schutz, Gen. Relativ. Gravit. **19**, 1163 (1987).

[8] D. Markovic, Phys. Rev. D **48**, 4738 (1993).

[9] For example, R. Narayan, B. Paczynski, and T. Piran, Astrophys. J. **395**, L83 (1992); T. Nakamura *et al.*, Prog. Theor. Phys. **87**, 879 (1992), and references therein.

[10] C. M. Will, *Theory and Experiment in Gravitational Physics* (Cambridge University Press, Cambridge, England, 1992), and references therein.

[11] J. H. Taylor and J. M. Weisberg, Astrophys. J. **345**, 434 (1989); T. Damour and J. H. Taylor, Phys. Rev. D **45**, 1840 (1992).

[12] T. Damour and A. M. Polyakov, report (unpublished).

[13] C. Brans and R. H. Dicke, Phys. Rev. **124**, 925 (1961).

[14] C. M. Will and H. W. Zaglauer, Astrophys. J. **346**, 366 (1989).

[15] D. M. Eardley, D. L. Lee, and A. P. Lightman, Phys. Rev. D **8**, 3308 (1973).

[16] D. L. Lee, Phys. Rev. D **10**, 2374 (1974).

[17] R. Monchmeyer *et al.*, Astron. Astrophys. **256**, 417 (1991); L. S. Finn, Ann. N. Y. Acad. Sci. **631**, 156 (1991).

[18] H. W. Zaglauer, Astrophys. J. **393**, 685 (1992).

[19] S. W. Hawking, Commun. Math. Phys. **25**, 167 (1972); Y. Suzuki and M. Yoshimura, Phys. Rev. D **43**, 2549 (1991).

[20] R. H. Dicke, Phys. Rev. **125**, 2163 (1962).

[21] W. H. Press *et al.*, *Numerical Recipes* (Cambridge University Press, Cambridge, England, 1989).

[22] L. I. Petrich, S. L. Shaprio, and S. A. Teukolsky, Phys. Rev. D **31**, 2459 (1985).

[23] D. M. Eardley and L. Smarr, Phys. Rev. D **19**, 2239 (1979).

[24] S. L. Shapiro and S. A. Teukolsky, *Black Holes, White Dwarfs and Neutron* Stars (Wiley-Interscience, New York, 1983).

[25] T. Matsuda and H. Nariai, Prog. Theor. Phys. **49**, 1195 (1973).

[26] T. Nakamura, K. Oohara, and Y. Kojima, Prog. Theor. Phys. Suppl. **99**, 110 (1987).

[27] B. F. Schutz and C. M. Will, Astrophys. J. **291**, L33 (1985).

[28] R. F. Stark and T. Piran, Phys. Rev. Lett. **55**, 891 (1985).

[29] L. Lindblom and S. L. Detweiler, Astrophys. J. Suppl. **53**, 73 (1983).

[30] R. M. Wald, *General Relativity* (University of Chicago Press, Chicago, 1984).